scientific reports

Check for updates

OPEN

Graphene–oxide interface for optoelectronic synapse application

Ricardo Martinez-Martinez[1,2], Molla Manjurul Islam[1,3], Adithi Krishnaprasad[1,2] & Tania Roy[1,2,3,4]✉

Optoelectronic synapses combine the functionalities of a non-volatile memory and photodetection in the same device, paving the path for the realization of artificial retina systems which can capture, pre-process, and identify images on the same platform. Graphene/Ta_2O_5/graphene phototransistor exhibits synapse characteristics when visible electromagnetic radiation of wavelength 405 nm illuminates the device. The photocurrent is retained after light withdrawal when positive gate voltage is applied to the device. The device exhibits distinct conductance states, modulated by different parameters of incident light, such as pulse width and number of pulses. The conductance state can be retained for 10^4 s, indicating long term potentiation (LTP), similar to biological synapses. By using optical and electrical pulses, the device shows optical potentiation and electrical LTD repeatably, implying their applicability in neural networks for pattern recognition.

The miniaturization of digital components is reaching the limits predicted by Moore's law, and new methodologies and devices that can collect, store and process information have been pursued. Motivated by the brain's ability to store, process, and memorize information, neuromorphic computing rises as an active candidate to solve the miniaturization problem. Neuromorphic computing contrasts with traditional von Neumann architecture due to the well-suited interaction with sensory data in humanlike ways[1–4]. In biological brains, neuron and synapses are the smallest units of learning and memory. To do neuromorphic computing, the realization of neurons and synapses is necessary. Memristors have reached an advance stage of exploration for mimicry electronic synapses[5–8]. However, since most of the information sensed and stored by the brain comes from the eyes, a pure electrical synapse is not sufficient; an optoelectronic synapse is going to fulfill more necessities in the internet of things (IoT) and big-data era. For example, Chen et al.[9,10], have shown an avalanche photodetector in the mid-wavelength infrared region (MWIR), which is important for remote sensing and defense[11] because of its transparency in the Earth's atmosphere; employing this type of photodetectors on optoelectronic synapses can improve the way for future pattern recognition applications. For the realization of an artificial retina, platforms integrating diffractive optics are required but chromatic aberration is a problem when using diffractive optics in such small scales. The work by Ou et al.[12], shows an achromatic metasurface in the MWIR wavelengths compatible with CMOS platform[13]. By proper material engineering, the integration of this metasurfaces can help with the realization of artificial retina systems. Such multifunctional devices can perform photodetection and store the information carried by light signals, such as wavelength and intensity, as conductance states.

Realization of optoelectronic synaptic devices have been possible using 2D materials such as MoS_2, WS_2 and WSe_2[14–18]. Graphene is another 2D material with unique optoelectronic properties that has not been fully explored for optoelectronic synapse applications. Graphene is a gapless two-dimensional (2D) material which exhibits an absorption spectrum from ultra-violet to terahertz wavelengths; it shows very large mobility and ambipolar characteristics[19–23]. Single-layer graphene absorbs only ~ 2.3% in visible and infrared regions and because of the zero band-gap behavior on the energy diagram, it leads to short lifetime of exciton in pure graphene; the high carrier mobility (electrons and holes) comes with the price of low light absorption, which gives low responsivity values (1 mA/W)[24,25]. Due to the semimetallic nature of graphene, a standard graphene field effect transistors with a graphene channel between two electrodes, can result in high dark current approaching the microampere regime which is an obstruction on many applications because of the increase in shot noise[26,27]. Hybrid graphene-quantum dot structures[26,28,29], artificial nanostructures on graphene[30] and functionalization

[1]NanoScience Technology Center, University of Central Florida, Orlando, FL 32826, USA. [2]Department of Electrical and Computer Engineering, University of Central Florida, Orlando, FL 32816, USA. [3]Department of Physics, University of Central Florida, Orlando, FL 32816, USA. [4]Department of Materials Science and Engineering, University of Central Florida, Orlando, FL 32816, USA. ✉email: tania.roy@ucf.edu

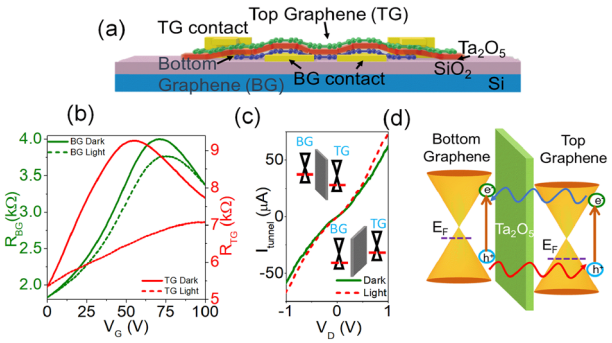

Figure 1. Graphene/Ta_2O_5/graphene (**a**) device schematic (not to scale). (**b**) *R vs.* V_G for bottom (R_{BG}) and top (R_{TG}) graphene in dark and under illumination of 405 nm wavelength. (**c**) Tunneling current from top graphene to bottom graphene layer as a function of drain source voltage V_D between the two layers, while the substrate experiences a global back-gate voltage of 80 V, in dark and under illumination. The dielectric strength of SiO_2 is 10^7 V/cm and for Ta_2O_5 is 8×10^6 V/cm[43]. (**d**) Band diagram of graphene/Ta_2O_5/graphene heterostructure highlighting the mechanism of photocurrent generation on top graphene layer.

of graphene[31] have been used to increase the carrier lifetime in graphene-based photodetectors. Unfortunately, the use of quantum dots or nanostructures constrains the inherent wide absorption of graphene to that specific range of the assisted structure. Liu et al. used a dielectric layer between two monolayer graphene films to enhance the photocurrent by photogating effect caused by tunneling of photogenerated carriers from one layer to the other[25]. Qin et al., used a hybrid phototransistor based on monolayer graphene on top of single-walled carbon nanotubes (SWNTs) on a SiO_2/Si substrate for optoelectronic synaptic device, the physical mechanism behind the operation being the interface trap between graphene and SWNTs[32]. Graphene-based optoelectronic synapse is also obtained by using 2D perovskite/graphene structure[33]. However, there has not been much exploration on the use of graphene/oxide interface for optoelectronic synapse which is important because it can get integrated easily with CMOS technology.

In this work, we use a graphene/Ta_2O_5/graphene heterostructure to demonstrate optoelectronic synapses. Ta_2O_5 has shown good platform on CMOS technology[34,35]. It also has a high energy bandgap of ~ 4 eV which facilitates the realization of optoelectronic synaptic characteristics in the visible spectrum[36]. It has been shown that Ta_2O_5 deposited by e-beam instead of RF sputtering gives a narrow gap of visible light absorption[34,35,37]. which is the mechanism used for deposition in this work. Graphene can show different mechanism for the change in current with light; photo-induced bolometric effect and photovoltaic[22]. In order to decouple these two effects, we used a Si/SiO_2 substrate with 285 nm thick dielectric as opposed to Freitag et al.[19] where the thickness of the dielectric is 90 nm. Probing the top graphene layer, we observe gate-controlled long-term potentiation (LTP) in these devices. A positive gate voltage is essential to enhance carrier lifetime, elongating the retention of photoconductance. The device exhibits distinct conductance states as a function of light pulse width and the number of light pulses applied. The device demonstrates LTP for $\geq 10^4$ s. It can be optically potentiated and electrically depressed to obtain its conductance weight update curves, essential for use in neural networks for pattern recognition.

Results and discussion

The graphene/Ta_2O_5/graphene device schematic is shown in Fig. 1a. The fabrication process is described thoroughly on the experimental section. Figure 1b shows the *R vs.* V_G characteristics of the bottom and top graphene films with the gate voltage applied through the Si substrate which we are going to refer as the global back gate voltage. Refer to methods for the thickness and doping of substrate. The hole mobility of the bottom graphene film in dark is calculated to be in the range of 1000–2272 cm^2/V-s and the contact resistance in the range of 281–717 Ω for 10 devices. Figure S3 shows the transfer characteristics of 6 different devices. In order to calculate the mobility, we fit the *R* vs V_G plot using the model[27,38]:

$$R = 2R_c + \frac{L}{Wq\mu} \frac{1}{\sqrt{n_0^2 + n_g^2}}$$

where $n_0 \sim \varepsilon_r \varepsilon V_g / te$ and at the charge neutrality point $R \approx 2R_c$[21,39].

The V_{CNP} of the top graphene layer is lower than that of the bottom graphene layer. This indicates that the bottom graphene film is more p-doped than the top graphene film, given that the effective electric field reaching the bottom graphene is higher than the top graphene because of the additional Ta_2O_5 layer between the two graphene layers. Upon illumination with light of wavelength 405 nm, with a power of 100 mW, the V_{CNP} of both the top and bottom graphene layers shift positively. Figure 1c shows the current flowing from the top graphene layer to the bottom graphene layer (I_{tunnel}) as a function of voltage applied across the two graphene layers, both in dark and under illumination, indicating the tunneling of carriers from one layer to the other across the Ta_2O_5 barrier. The tunneling current is enhanced upon illumination. During illumination, the bottom graphene layer generates electron–hole pairs. Since the bottom graphene layer has a higher charge neutrality point V_{CNP} than

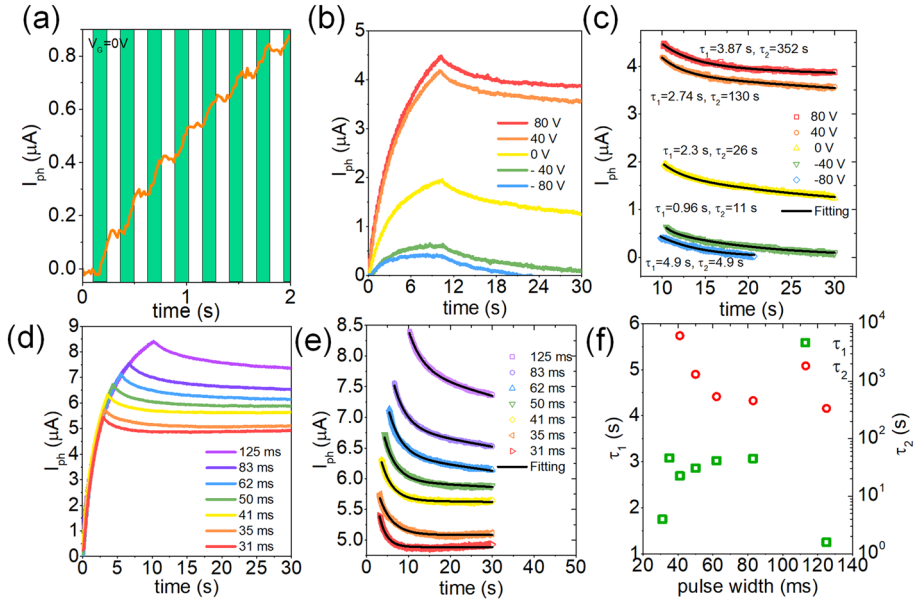

Figure 2. (**a**) Photocurrent measured across the top graphene layer as a function of time, when pulses of light (λ = 405 nm), of duration t_{ON} = 125 ms, t_{OFF} = 125 ms, are incident on the device. (**b**) Photocurrent measured across top graphene layer as a function of time, with varying back gate voltage. (**c**) Photocurrent retained after withdrawal of light as a function of time, fitted with a double exponential, indicating a fast decay with time constant τ_1 followed by a slow decay of current with a time constant of τ_2. (**d**) Photocurrent as a function of time with varying light pulse width. V_G = 80 V, V_{TGr} = 0.1 V. (**e**) Retained photocurrent after light pulse withdrawal as a function of time from (**d**), fitted with a double exponential. (**f**) Photocurrent decay time constants τ_1 and τ_2, extracted from (**e**), as a function of pulse width.

the top graphene layer in dark, implying a higher hole doping in the bottom graphene layer, the photogenerated holes tunnel into the top graphene layer. The photogenerated electrons from the top graphene layer can also tunnel into the bottom graphene layer. The accumulation of electrons in the bottom graphene layer leads to a photogating effect, shifting the V_{CNP} of the top graphene layer to more positive voltages. This enhances the photocurrent in the top graphene layer significantly, as indicated by the decreased resistance of the top graphene layer upon illumination. Because of the large spot area of the laser light it could also mean that near the graphene/metal interface causes a bolometric effect which in turn increases the photo-generated current. The mechanism of enhanced carrier generation due to the presence of a tunneling barrier between the top and bottom graphene layers is illustrated through the band diagram in Fig. 1d. The positive shift in V_{CNP} of both bottom and top graphene layers under illumination can also be associated to the adsorption of water molecules in the Gr/Ta_2O_5 interface. This behavior is not observed in Liu et al., since RF sputtering creates a zero absorption Ta_2O_5 film[37].

Figure 2a shows the effect of a stream of light pulses of 405 nm wavelength and intensity of 63 mW/cm^2 incident on a typical graphene/Ta_2O_5/graphene device. The light pulses are 125 ms long. The back gate voltage V_G is held at 0 V. The bottom graphene is kept floating. A drain-source voltage of V_{TGr} = 0.1 V is applied to the top graphene layer. The dimensions of the bottom graphene layer is $L = 10\ \mu m$, $W = 5\ \mu m$ and the dimensions of the top graphene layer is $L = 44\ \mu m$, $W = 15\ \mu m$. The calculated responsivity from Fig. 1b is: for the bottom graphene $\mathcal{R}_b = 83.94$ mV/W, the calculated responsivity of top graphene is $\mathcal{R}_t = 1.17$ V/W.

The photocurrent is given by $I_{ph} = I_{light} - I_{dark}$, where I_{dark} is the current through the top graphene layer in dark, and I_{light} is the current after illumination with each light pulse (shown in Fig. S4a). We observe that I_{ph} increases with each light pulse, and during the off period of 125 ms between two consecutive light pulses, the photocurrent does not decay to the dark state, indicating short term potentiation (STP) of the device. Figure 2b shows the effect of global-gate voltage on the LTP of the device. The global-gate voltage is varied from − 80 to + 80 V. The gate voltage is varied from − 80 to + 80 V. 40 light pulses, each with a duration of 125 ms, are applied on the device. The photocurrent, measured on the top graphene layer, increases with each incident pulse for all gate voltages. When the light pulses are withdrawn, the conductance state decays for $V_G \leq 0$ V, indicating STP. The total current under illumination is shown in Fig. S4b. The decaying photocurrent can be fitted by a double exponential function $Y = y_0 + A_1\exp(-t/\tau_1) + A_2\exp(-t/\tau_2)$ as shown in Fig. 2c. Here y_0 is the offset, τ_1 and τ_2 are time constants for a fast and slow decay, respectively, and A_1 and A_2 are pre-exponentials. We observe that for all gate voltages, there is a fast (within ~ 3 s) decay in photocurrent. However, for positive gate voltages, there is a slow decay of conductance following that. The device is able to retain the conductance state for > 100 s. The photocurrent increases with increasing gate voltage, and the conductance retention increases as well. This is because, the positive back gate voltage helps in the trapping of electrons at the graphene/dielectric interfaces, leading to accumulation of holes in the top graphene layer. Figure 2d shows the effect of the light pulse width on the photocurrent and its retention. Figure S3c shows the total current under illumination. The pulse width is

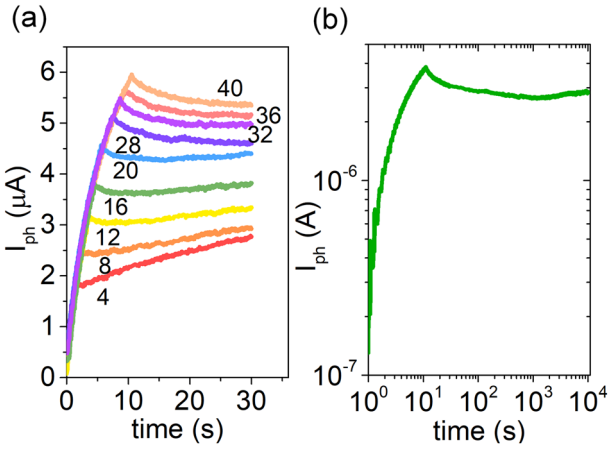

Figure 3. (**a**) Photocurrent across the top graphene layer as function of time for varying number of incident light pulses, wavelength = 405 nm, power = 100 mW, $t_{ON} = t_{OFF} = 125$ ms. (**b**) Long term potentiation for 10^4 s, with 40 light pulses. $V_G = 80$ V, $V_{TGr} = 0.1$ V.

varied from 31 to 125 ms. The photocurrent increases with increasing pulse width, as expected, and decays only gradually after the pulses are withdrawn. Again, the decaying photocurrent is fitted with the aforementioned double exponential function as shown in Fig. 2e. The photocurrent undergoes a fast decay initially within the first ~ 3 s of light pulse withdrawal, and then relaxes into a steady level which retains for > 100 s, with τ_2 reaching infinity for the pulse widths of 31 and 35 ms. The fitted time constants are plotted in Fig. 2f. This steady current level indicates the long-term potentiated conductance state of the device. These results illustrate that with a positive gate voltage, the Graphene/Ta_2O_5/Graphene devices can exhibit optically stimulated long term memory.

An electronic synapse shows multiple conductance states when subjected to electrical pulses. Similarly, a device behaves as an optoelectronic synapse when multiple non-volatile conductance states can be extracted as a function of number of incident optical pulses. Figure 3a shows the existence of 9 distinct conductance states for at least 20 s, in a typical Graphene/Ta_2O_5/Graphene device, as the number of light pulses is varied from 4 to 40. The gate voltage is held at + 80 V, and the photocurrent is measured from the top graphene layer held at a drain-source voltage (V_{TGr}) of 0.1 V. Figure S4a shows the total current measured. Figure 3b shows that the device is able to retain its conductance state for ~ 10^4 s after the application of 40 light pulses, each of duration 125 ms. The measured current through top graphene layer is shown in Fig. S4b. Typical electronic synapses exhibit a retention of > 10^3 s for use in neural networks. Thus, our graphene/Ta_2O_5/graphene device is fit for practical implementation in neural networks for learning and inference tasks.

A synaptic device's conductance tuning curve is of utmost importance for its use in the training of a neural network. Linearity and symmetry in conductance weight update determine the accuracy of the neural network. For obtaining the weight update of the graphene/Ta_2O_5/graphene optoelectronic synapses, we use 20 optical pulses of duration 125 ms to potentiate the device, and 20 electrical pulses at the gate electrode to depress the device. While optically potentiating the device, the gate voltage V_G is held at + 80 V for inducing a condition of maximum conductance retention. To depress the device, the light pulses are withdrawn, and V_G is pulsed from + 80 to + 70 V, with a 125 ms on time and 125 ms off time. The top graphene drain-source voltage V_{TGr} is held at 0.1 V throughout the measurement. The reduction of the gate voltage using pulses releases trapped electrons in gradual steps and reduces the conductance of the device gradually. Thus, the conductance weight update curve is obtained, as shown in Fig. 4. The optical potentiation—electrical depression cycle is repeated 3 times to show the reliability of the process. We extract the nonlinearity factor (NLF) and symmetry of the potentiation and depression curves using a behavioral model described by Chen et al. The NLF values are close to 1, indicating a high linearity in weight update. Additionally, the symmetry, given by $\left|NLF_{potentiation} - NLF_{depression}\right|$ ranges from 0.2 to 0.4, indicating an extremely symmetric weight update, which further aids in improving the accuracy of the network.

Conclusion

In summary, we report Graphene/Ta_2O_5/Graphene heterostructures acting as optoelectronic synapses. These devices show enhanced photocurrent due to photogating effect caused by selective tunneling of photogenerated carriers from one graphene layer to the other. The devices exhibit LTP, modulated by the gate voltage. The conductance states can be modulated by the light pulse width and the number of light pulses applied. The device retains its conductance state for 10^4 s. Optical potentiation and electrical depression can be repeatably used to generate conductance weight update curves for these devices, to be used for the training of neural networks for pattern recognition tasks.

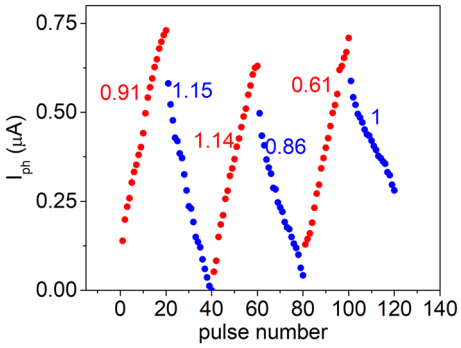

Figure 4. Weight update characteristics. Optical potentiation is obtained with 20 light pulses of $t_{ON} = t_{OFF} = 125$ ms, $\lambda = 405$ nm, $V_G = 80$ V, $V_{TGr} = 0.1$ V. Electrical depression is obtained in dark, keeping V_{TGr} at 0.1 V, and pulsing the gate voltage from 80 to 70 V, with a pulse width of 125 ms, using 20 voltage pulses. The cycle is repeated 3 times. Non-linearity factors for potentiation and depression are included in the plots.

Methods

Materials and device fabrication. We first pattern the bottom graphene electrodes on a p-Si/SiO_2 (285 nm) substrate, which acts as the global back gate, by standard photolithography technique, and deposit Ni/Au (60/20 nm) by electron beam evaporation followed by lift-off. A monolayer of graphene film, grown by chemical vapor deposition (CVD) on Cu foil is wet-transferred onto this substrate[40], followed by annealing in forming gas (10% H_2, 90% N_2) for 3 h at 400 °C. The bottom graphene layer is patterned and etched in O_2 plasma to form graphene strips. Next, 5 nm of Ta_2O_5 is patterned and deposited by e-beam evaporation. A second monolayer of CVD-grown graphene is wet-transferred on the substrate, patterned and etched into strips aligned with the bottom graphene layer. Ni/Au electrodes are patterned and deposited as contacts to the top graphene layer. Finally, the devices are annealed again in forming gas for 3 h at 300 °C.

Device characterization. The optical image of a representative device with 5 terminals is shown in Fig. S1. The atomic force microscope (AFM) height profile shown in Fig. S2a confirms the thickness of the Ta_2O_5 film to be 5 nm. Figure S2b,c shows the Raman spectrum of the bottom and top graphene layers confirming that they are of monolayer thickness[41,42]. All electrical measurements were performed at room temperature on a probe station, using HP 4145B Semiconductor Parameter Analyzer and B1500A Semiconductor Device Analyzer. To measure the transfer characteristics after illumination of light, we use a cw laser diode light source in the visible spectrum radiation ($\lambda_0 = 405$ nm) where light propagates in free space (spot size 0.55 cm). For light pulses, the laser light travels through an optical fiber (77,563 newport fused silica) with a transmittance of 45% (spot area ≈ 0.714 cm^2).

Data availability

All data generated and analyzed during this study are either included in the published article itself (or available within the Supplementary Information files).

Received: 7 January 2022; Accepted: 21 March 2022
Published online: 07 April 2022

References

1. Shepherd, G. M. *The Synaptic Organization of the Brain* (Oxford University Press, 2004).
2. Merolla, P. A. *et al.* A million spiking-neuron integrated circuit with a scalable communication network and interface. *Science* **345**, 668–673 (2014).
3. Prezioso, M. *et al.* Training and operation of an integrated neuromorphic network based on metal-oxide memristors. *Nature* **521**, 61–64. https://doi.org/10.1038/nature14441 (2015).
4. Koelmans, W. W. *et al.* Projected phase-change memory devices. *Nat. Commun.* **6**, 1–7 (2015).
5. Zhao, H. *et al.* Atomically thin femtojoule memristive device. *Adv. Mater.* **29**, 1703232 (2017).
6. Feng, X. *et al.* A fully printed flexible MoS_2 memristive artificial synapse with femtojoule switching energy. *Adv. Electron. Mater.* **5**, 1900740 (2019).
7. Xu, R. *et al.* Vertical MoS_2 double-layer memristor with electrochemical metallization as an atomic-scale synapse with switching thresholds approaching 100 mV. *Nano Lett.* **19**, 2411–2417 (2019).
8. Wang, K. *et al.* A pure 2H-MoS_2 nanosheet-based memristor with low power consumption and linear multilevel storage for artificial synapse emulator. *Adv. Electron. Mater.* **6**, 1901342 (2020).
9. Chen, J. *et al.* Uniformly broadband far-infrared response from the photocarrier tunneling of mesa Si: P blocked-impurity-band detector. *IEEE Trans. Electron Devices* **68**, 560–564 (2020).
10. Chen, J. *et al.* High-performance HgCdTe avalanche photodetector enabled with suppression of band-to-band tunneling effect in mid-wavelength infrared. *npj Quant. Mater.* **6**, 1–7 (2021).
11. Chen, J. *et al.* Recent progress in improving the performance of infrared photodetectors via optical field manipulations. *Sensors* **22**, 677 (2022).
12. Ou, K. *et al.* Mid-infrared polarization-controlled broadband achromatic metadevice. *Sci. Adv.* **6**, eabc0711 (2020).
13. Ou, K. *et al.* Broadband achromatic metalens in mid-wavelength infrared. *Laser Photonics Rev.* **15**, 2100020 (2021).

14. He, H. K. *et al.* Photonic potentiation and electric habituation in ultrathin memristive synapses based on monolayer MoS_2. *Small* **14**, 1800079 (2018).
15. Seo, S. *et al.* Artificial optic-neural synapse for colored and color-mixed pattern recognition. *Nat. Commun.* **9**, 1–8 (2018).
16. Islam, M. M., Dev, D., Krishnaprasad, A., Tetard, L. & Roy, T. Optoelectronic synapse using monolayer MoS_2 field effect transistors. *Sci. Rep.* **10**, 1–9 (2020).
17. Wang, C.-Y. *et al.* Gate-tunable van der Waals heterostructure for reconfigurable neural network vision sensor. *Sci. Adv.* **6**, eaba6173 (2020).
18. Abnavi, A. *et al.* Free-standing multilayer molybdenum disulfide memristor for brain-inspired neuromorphic applications. *ACS Appl. Mater. Interfaces.* **13**, 45843–45853 (2021).
19. Freitag, M., Low, T., Xia, F. & Avouris, P. Photoconductivity of biased graphene. *Nat. Photonics* **7**, 53 (2013).
20. Zhan, B. *et al.* Graphene field-effect transistor and its application for electronic sensing. *Small* **10**, 4042–4065 (2014).
21. Novoselov, K. S. *et al.* Electric field effect in atomically thin carbon films. *Science* **306**, 666–669 (2004).
22. Koppens, F. *et al.* Photodetectors based on graphene, other two-dimensional materials and hybrid systems. *Nat. Nanotechnol.* **9**, 780–793 (2014).
23. Novoselov, K., Mishchenko, O. A., Carvalho, O. A. & Neto, A. C. 2D materials and van der Waals heterostructures. *Science* **353**, aac9439 (2016).
24. Xia, F. *et al.* Photocurrent imaging and efficient photon detection in a graphene transistor. *Nano Lett.* **9**, 1039–1044 (2009).
25. Liu, C.-H., Chang, Y.-C., Norris, T. B. & Zhong, Z. Graphene photodetectors with ultra-broadband and high responsivity at room temperature. *Nat. Nanotechnol.* **9**, 273–278 (2014).
26. De Fazio, D. *et al.* Graphene-quantum dot hybrid photodetectors with low dark-current readout. *ACS Nano* **14**, 11897–11905 (2020).
27. Wang, Y., Ho, V. X., Henschel, Z. N., Cooney, M. P. & Vinh, N. Q. Effect of high-κ dielectric layer on 1/f noise behavior in graphene field-effect transistors. *ACS Appl. Nano Mater.* **4**, 3647–3653 (2021).
28. Konstantatos, G. *et al.* Hybrid graphene–quantum dot phototransistors with ultrahigh gain. *Nat. Nanotechnol.* **7**, 363–368. https://doi.org/10.1038/nnano.2012.60 (2012).
29. Sun, Z. *et al.* Infrared photodetectors based on CVD-grown graphene and PbS quantum dots with ultrahigh responsivity. *Adv. Mater.* **24**, 5878–5883. https://doi.org/10.1002/adma.201202220 (2012).
30. Zhang, B. Y. *et al.* Broadband high photoresponse from pure monolayer graphene photodetector. *Nat. Commun.* **4**, 1811. https://doi.org/10.1038/ncomms2830 (2013).
31. Chitara, B., Panchakarla, L., Krupanidhi, S. & Rao, C. Infrared photodetectors based on reduced graphene oxide and graphene nanoribbons. *Adv. Mater.* **23**, 5419–5424 (2011).
32. Qin, S. *et al.* A light-stimulated synaptic device based on graphene hybrid phototransistor. *2D Materials* **4**, 035022 (2017).
33. Tian, H., Wang, X., Wu, F., Yang, Y. & Ren, T. In *2018 IEEE International Electron Devices Meeting (IEDM).* 38.36.31–38.36.34.
34. Atanassova, E., Dimitrova, T. & Koprinarova, J. AES and XPS study of thin RF-sputtered Ta_2O_5 layers. *Appl. Surf. Sci.* **84**, 193–202 (1995).
35. Todorova, Z. *et al.* Electrical and optical characteristics of Ta_2O_5 thin films deposited by electron-beam vapor deposition. *Plasma Process. Polym.* **3**, 174–178 (2006).
36. Chen, X., Bai, R. & Huang, M. Optical properties of amorphous Ta_2O_5 thin films deposited by RF magnetron sputtering. *Opt. Mater.* **97**, 109404 (2019).
37. Kulpa, A. & Jaeger, N. A. Comparison of the optical properties of tantalum pentoxide, Ta_2O_5, anodically grown from E-beam deposited tantalum, Ta, with Ta_2O_5 E-beam deposited from a Ta_2O_5 source. *ECS Trans.* **41**, 311 (2011).
38. Kim, S. *et al.* Realization of a high mobility dual-gated graphene field-effect transistor with Al_2O_3 dielectric. *Appl. Phys. Lett.* **94**, 062107 (2009).
39. Nagashio, K., Nishimura, T. & Toriumi, A. Estimation of residual carrier density near the Dirac point in graphene through quantum capacitance measurement. *Appl. Phys. Lett.* **102**, 173507 (2013).
40. Chan, J. *et al.* Reducing extrinsic performance-limiting factors in graphene grown by chemical vapor deposition. *ACS Nano* **6**, 3224–3229. https://doi.org/10.1021/nn300107f (2012).
41. Ni, Z., Wang, Y., Yu, T. & Shen, Z. Raman spectroscopy and imaging of graphene. *Nano Res.* **1**, 273–291 (2008).
42. Malard, L., Pimenta, M. A., Dresselhaus, G. & Dresselhaus, M. Raman spectroscopy in graphene. *Phys. Rep.* **473**, 51–87 (2009).
43. Chaneliere, C., Autran, J., Devine, R. & Balland, B. Tantalum pentoxide (Ta2O5) thin films for advanced dielectric applications. *Mater. Sci. Eng. R. Rep.* **22**, 269–322 (1998).

Acknowledgements

This work was supported by NSF-ECCS-1845331 (CAREER) and AFOSR through award number FA8651-20-1-0008.

Author contributions

R.M.M. and T.R. conceived the project and T.R. directed it. A.K. performed the graphene transfer process. M.M.I. performed the AFM and Raman spectroscopy. A.K. and M.M.I assisted R.M.M. with the electrical characterizations. R.M.M and T.R. wrote the manuscript with inputs from all authors.

Competing interests

The authors declare no competing interests.

Additional information

Supplementary Information The online version contains supplementary material available at https://doi.org/10.1038/s41598-022-09873-8.

Correspondence and requests for materials should be addressed to T.R.

Reprints and permissions information is available at www.nature.com/reprints.

Publisher's note Springer Nature remains neutral with regard to jurisdictional claims in published maps and institutional affiliations.